JOURNAL OF GEOPHYSICAL RESEARCH, VOL. 99, NO. C12, PAGES 24,915–24,926, DECEMBER 15, 1994

TOPEX/POSEIDON microwave radiometer performance and in-flight calibration

Christopher S. Ruf,[1] Stephen J. Keihm,[2] Bala Subramanya,[1,3] and Michael A. Janssen[4]

Abstract. Results of the in-flight calibration and performance evaluation campaign for the TOPEX/POSEIDON microwave radiometer (TMR) are presented. Intercomparisons are made between TMR and various sources of ground truth, including ground-based microwave water vapor radiometers, radiosondes, global climatological models, special sensor microwave imager data over the Amazon rain forest, and models of clear, calm, subpolar ocean regions. After correcting for preflight errors in the processing of thermal/vacuum data, relative channel offsets in the open ocean TMR brightness temperatures were noted at the ≈1 K level for the three TMR frequencies. Larger absolute offsets of 6–9 K over the rain forest indicated a ≈5% gain error in the three channel calibrations. This was corrected by adjusting the antenna pattern correction (APC) algorithm. A 10% scale error in the TMR path delay estimates, relative to coincident radiosondes, was corrected in part by the APC adjustment and in part by a 5% modification to the value assumed for the 22.235 GHz water vapor line strength in the path delay retrieval algorithm. After all in-flight corrections to the calibration, TMR global retrieval accuracy for the wet tropospheric range correction is estimated at 1.1 cm RMS with consistent performance under clear, cloudy, and windy conditions.

1. Introduction

The TOPEX/POSEIDON (T/P) satellite is a joint venture by NASA and the French space agency Centre National d'Etudes Spatiales (CNES) which is designed to produce global maps of ocean surface topography [*Stewart et al.*, 1986]. It was launched on August 10, 1992, and began operational data taking on September 23, 1992. The primary instruments on the satellite are two radar altimeters. The TOPEX/POSEIDON microwave radiometer (TMR) is included to monitor and correct for the electrical range delay (henceforth referred to as path delay) of the altimeter radar signal due to water vapor and cloud liquid water in the troposphere. In-flight calibration of the TMR is based on intercomparison studies between TMR data acquired during the first 6 months of operation and various sources of "ground truth" which were measured or modeled during satellite overpasses of selected ground sites. The results of those intercomparison studies are presented here.

TMR is a modified version of the scanning multichannel microwave radiometer (SMMR) which flew on Seasat and Nimbus-7 [*Swanson and Riley*, 1980]. TMR was restricted to operate at 18, 21, and 37 GHz and only in a nadir-viewing direction, which is coaligned with the radar altimeters, in order to accommodate the T/P mission requirements. The main antenna is a partially offset parabolic reflector with a projected aperture of 79 cm. This results in a footprint diameter on the ground of 43.4, 36.4, and 22.9 km at 18, 21, and 37 GHz, respectively. By comparison, the altimeter footprint is approximately 3 km in diameter. TMR operating characteristics are summarized in Table 1. A detailed description of the instrument is given by *Ruf et al.* [1994].

The conversion of raw TMR data into path delay corrections can be broken into three distinct steps. The raw data is first converted into antenna temperatures using data measured while viewing an ambient load and cold space. Antenna temperature calibration corrects for drifts in the radiometer gain and bias [*Ruf et al.*, 1994]. Secondly, the antenna temperatures are corrected for contributions from the sidelobes of the antenna radiation pattern by a procedure referred to as antenna pattern correction [*Janssen et al.*, 1994]. The percentage of power received by the antenna from its on-Earth and off-Earth sidelobes is determined from measurements of the radiation pattern on a far field antenna range prior to launch. These fractional powers, when combined with estimates of the mean on- and off-Earth brightness temperatures, are subtracted from the antenna temperature, resulting in the brightness temperature referred to the antenna main beam. This brightness temperature calibration is effectively a gain and bias correction to the antenna temperature. Thirdly, brightness temperatures at the three TMR frequencies are converted to path delay estimates by a path delay retrieval algorithm [*Keihm et al.*, 1994]. The retrieval essentially inverts the integral equation of radiative transfer to extract the water content of the atmosphere from the measured emissive effects of the water. The water content is then related to the path delay by its refractive properties. Uncertainties in the strength of the water vapor absorption line centered at 22.235 GHz, on which the

[1]Department of Electrical Engineering, Pennsylvania State University, University Park.
[2]Ball Corporation, Pasadena, California.
[3]Now at Hughes STX, Lanham, Maryland.
[4]Jet Propulsion Laboratory, California Institute of Technology, Pasadena.

Copyright 1994 by the American Geophysical Union.

Paper number 94JC00717.
0148-0227/94/94JC-00717$05.00

Table 1. TOPEX/POSEIDON Microwave Radiometer Engineering Specifications

	Frequency, GHz			
	18	21A	21B*	37
HPBW, deg	1.86	1.56	1.59	0.98
Footprint, km	43.4	36.4	37.1	22.9
Beam efficiency, %	91.1	89.3	87.4	90.5
Integration time, s	1.0	1.0	1.0	1.0
Radiometer noise, ΔT, K	0.26	0.27	0.27	0.27
TA accuracy,† K	0.57	0.57	0.54	0.54
Preflight T_B accuracy,‡ K	0.77	0.74	0.79	0.71
In-flight T_B accuracy, K	1.5	1.5	1.5	1.5

*Channel 21B is a backup channel. It was not used during the verification phase of the mission.

†Antenna temperature calibration accuracy does not include the antenna pattern corrections [*Ruf et al.*, 1994].

‡Preflight brightness temperature accuracy refers to the predicted TMR performance, assuming representative antenna pattern measurements [*Janssen et al.*, 1994]. The addition of thermal blanketing around the antenna feed prior to launch necessitated in-flight adjustments to the far sidelobe levels, which introduced additional uncertainties into the brightness temperature calibration algorithm.

emissive behavior of the water depends, introduces an uncertainty into the "gain" of the path delay retrieval algorithm.

Because all three of the data processing steps described above are essentially linear operations, gain errors in the antenna and brightness temperature calibration will affect the final path delay estimates in the same way as the line strength uncertainty. Similarly, biases in the calibrated brightness temperatures may be due to errors in either the antenna or the brightness temperature calibration procedures. The in-flight calibration described below estimates the gain and bias errors through intercomparisons with various sources of ground truth. An attempt is also made to identify the sources of these errors, so that the proper step in the calibration procedure can be adjusted accordingly. The intent of this approach is to produce both accurate path delay corrections, for use by the radar altimeters, and accurate brightness temperatures, for use in related research areas. Possible uses for well-calibrated nadir viewing brightness temperatures include studies of two- versus three-frequency path delay retrieval algorithms, refinements to the model for sea surface excess emissivity as a function of wind speed, and corrections to the water vapor line strength.

This paper is divided into six sections. In section 2 the sensitivity of the antenna temperature calibration to varying thermal environments is evaluated. This issue had a significant negative impact on the SMMR performance, and the effectiveness of several modifications to TMR, which were made based on lessons learned from SMMR, is assessed. Section 3 reviews the various sources of ground truth data used in this study. Included are ground-based microwave water vapor radiometer (WVR) and radiosonde measurements, climatological model data, Defense Meteorological Satellite Program special sensor microwave/imager (SSM/I) data over the Amazon rain forest, and a reference brightness temperature model for clear, calm, subpolar ocean regions. Section 4 describes the changes which were made in the antenna and brightness temperature calibration procedures to correct for bias and gain errors due to instrument effects. Section 5 describes the changes which were made in the path delay retrieval algorithm to correct for scale errors due to water vapor line strength uncertainties. Section 6 concludes with an overall assessment of the accuracy of the brightness temperature and path delay estimates produced by TMR.

2. Instrument Thermal Performance

SMMR calibration was adversely affected by large temperature variations in the cold sky waveguide and antenna and in the main antenna feed [*Francis*, 1987; *Milman and Wilheit*, 1985]. A number of modifications to SMMR were made to reduce the sensitivity of the antenna temperature calibration to the on-orbit thermal environment. Polystyrene radomes were placed in front of both the main antenna feed and the cold sky horns. Yaw maneuvers of the spacecraft were incorporated into the operational orbit to keep TMR on the shade side of the satellite. The cold sky horns were also positioned on the instrument so as to minimize exposure to direct sunlight. In addition, preflight calibration of the models used to correct for the emissive and absorptive effects of the radiometer hardware was more extensive in the case of TMR. A detailed description of the TMR hardware modifications and of the changes in the preflight calibration are given by *Ruf et al.* [1994].

A time series of the physical temperature of TMR during the first 6 months of flight is shown in Figure 1. This temperature sensor is located in the heart of the microwave electronics subsystem for the primary 21-GHz channel, and represents a good estimate of the overall temperature of the critical electronics. A periodicity is evident in the time series which repeats approximately every 60–70 days. This is caused by the periodic variation of the solar "β-angle", the angle between the orbit plane and a line from the Earth to the Sun. β angles outside of ±20° correspond to the lower range of instrument temperatures (for example, from ≈65–110 days in Figure 1). Over this range of β the yaw orientation of the spacecraft is continually adjusted during each orbit to maintain good exposure of the solar panel to sunlight and to keep TMR in the shade of the spacecraft. The minimum temperatures occur at $\beta \approx 90°$. For β angles within ±20°, yaw maneuvers are disabled because the maneuver rate would be too fast. This results in the higher temperature peaks in Figure 1 (for example, from ≈45–60 days). Exten-

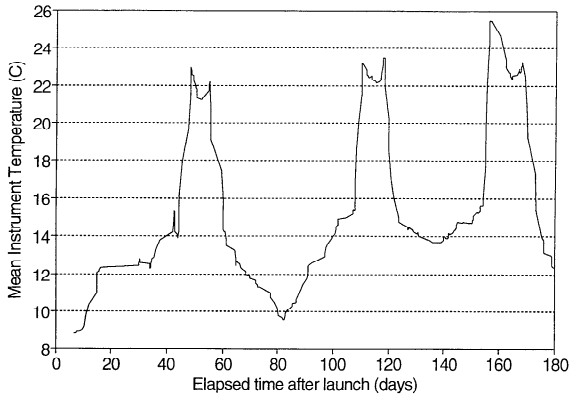

Figure 1. Time series of TMR instrument temperature during the first 6 months of the mission. The periodic minima and maxima are caused by variations in the orbit geometry and solar shading, as discussed in the text.

sive preflight performance evaluations of TMR were conducted over the range 5°–45°C. A second-order nonlinear instrument response was noted at that time which varied with the physical temperature of the instrument. This effect was modeled in the antenna temperature calibration procedure, which makes the quality of the calibration slightly dependent on the operating temperature of the instrument [*Ruf et al.*, 1994]. The in-flight temperatures are seen to lie comfortably within the preflight test range.

Francis [1987] showed that the most significant temperature-induced degradation in SMMR performance occurred during the shade-to-sun transition of each orbit. Figure 2a shows a ≈0.015 K/s variation in the temperature of the SMMR antenna feed during this time. In contrast, Figure 2b shows a ≈0.001 K/s temperature variation for TMR during the same transition period. This large reduction in the coupling between incident solar radiation and instrument temperature is due primarily to the incorporation of radomes over the antennas [*Linn*, 1992].

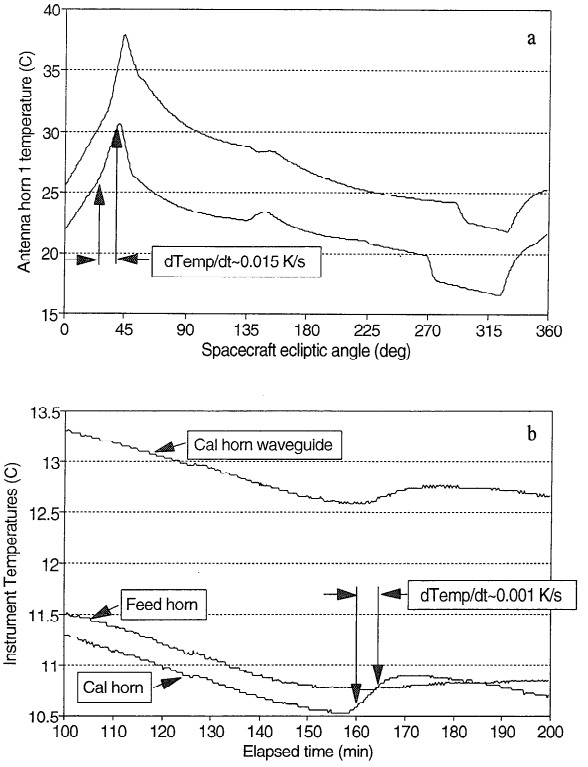

Figure 2. Time series of front-end microwave components critical to the antenna temperature calibration during one orbit. (a) Main reflector feed horn on the Nimbus-7 scanning multichannel microwave radiometer (SMMR) for two typical orbits over the course of the mission [after *Francis*, 1987]. (b) Feed horn, cold sky (cal) horn, and cal horn waveguide on TOPEX/POSEIDON microwave radiometer (TMR) for one typical orbit on day 246 (September 2, 1992). The largest temperature changes occur during the shade-to-sun transition in the orbit, at 0°–45° ecliptic angle for SMMR and at 160–165 min for TMR. Temperature changes on TMR have been greatly reduced by the inclusion of polystyrene radomes over the feed horn and cold sky horn.

3. Ground Truth Database

Water Vapor Radiometers

Ground-based microwave water vapor radiometers (WVRs) were deployed on the islands of Lampedusa, Italy (35.57N, 12.57E), Chichi Jima, Japan (27.08N, 142.18E), and Norfolk, Australia (29.03S, 167.93E) and on the Texaco oil platform Harvest (34.47N, 239.32E), 11 km from the California coastline. These sites all lie near the satellite ground track. The WVRs deployed at Lampedusa and Harvest operate at 20.7, 22.2, and 31.4 GHz. The single WVR deployed first at Chichi Jima and then at Norfolk operates at 20.7 and 31.4 GHz. All three WVRs achieve an absolute calibration accuracy in their brightness temperature measurements of approximately 0.5 K [*Keihm*, 1991]. This corresponds to an accuracy in the retrieval of path delay of approximately 0.25 cm due to instrument effects alone.

Lampedusa and Harvest are the primary altimeter validation sites for CNES and NASA, respectively. WVRs were deployed there in part to calibrate TMR and in part to assist with the atmospheric corrections during the altimeter intercomparisons. Norfolk and Chichi Jima were selected as additional temporary WVR sites exclusively for comparison with the TMR. Norfolk lies 29 km from an ascending node ground track and Chichi Jima lies 33 km from an ascending and 50 km from a descending node. A single WVR was deployed first at Chichi Jima during September of 1992, then relocated to Norfolk for comparisons through November 15, 1992. During this time, intercomparison data were obtained for 12 overpasses. Of this data, 11 overpasses occurred under cloud free and light wind (<7 m/s) conditions.

WVR intercomparisons with the TMR were made primarily between brightness temperatures, since this is the direct measurement made by the WVRs and the comparisons are unaffected by assumptions made regarding the vapor absorption line strength. Clear, calm conditions were preferred in the intercomparison analysis since cloud effects are highly variable spatially, and windy conditions introduce an added uncertainty into the estimate of the ocean surface contribution to the TMR brightness temperatures. Zenith brightness temperatures measured by the WVR 20.7-GHz channel ranged over 12–52 K for the clear, calm data, corresponding to a variation in path delay of 4–24 cm. From the WVR data an estimate can be made of the coincident brightness temperature as seen by TMR. This estimate utilizes a well-constrained model for the water vapor line shape and takes into account the temperature and emissivity of the ocean surface. The TMR brightness temperature can be expressed as

$$\mathrm{TB_{TMR}} = \varepsilon T_S e^{-\tau} + \mathrm{TB_{UP}} + (\mathrm{TB_{DN}} + T_C e^{-\tau})(1 - \varepsilon) e^{-\tau} \quad (1)$$

where ε is the calm water emissivity, T_S is the sea surface temperature in kelvins, τ is the atmospheric opacity, $\mathrm{TB_{UP}}$ and $\mathrm{TB_{DN}}$ are the upwelling and downwelling components of the atmospheric emission, and T_C is the cosmic background brightness temperature. The WVR measurements can be used to predict τ, $\mathrm{TB_{UP}}$, and $\mathrm{TB_{DN}}$ at the TMR frequencies. On the basis of regression fits to computations from a 4-year Bermuda radiosonde data set, we use

$$\tau_{18} = 0.0113 + 0.00076\mathrm{TB_{WVR21}} - 0.00008\mathrm{TB_{WVR22}} + 0.00132\mathrm{TB_{WVR31}} - 0.00005T_A \quad (2a)$$

Table 2. Radiosonde Intercomparison Database

Station Name	Latitude, °N	Longitude, °E	Average Path Delay, cm	Closest Approach, km
Port Blair	11.67	92.72	24.5	10/132/158
Hachijojima	33.10	139.78	10.4	40/108/130/201
Naze-On-Amami	28.38	129.50	13.4	14/240/266
Naha	26.12	127.40	16.6	26/41/221/242
Minamidaito Jima	25.83	131.23	11.4	48/139
Chichi Jima	27.08	142.18	15.7	32/49/208/228
Minamitorishima	24.30	153.97	18.4	30/68/196/237
Gough Island	−40.35	−9.88	12.5	42/48/253/284
Marion Island	−46.88	37.87	13.3	26/74/158/248
St. Paul Island	57.15	−170.22	6.3	36/72/148/196
Sable Island	43.93	−60.02	7.3	9/77/118/187
Bermuda NAS	32.37	−64.68	15.0	44/200/288
Juliana Airport	18.05	−63.12	18.1	250
Grantley Adams	13.07	−59.48	24.0	15/23/265
Andersen Air Force Base, Guam	13.33	144.50	19.2	26/27/261

Closest approach values are typical distances from satellite ground track to radiosonde launch site. Multiple values correspond to different ascending and descending orbit passes within 300 km of the launch site which coincided with an actual radiosonde launch. Closest approach values for individual overpasses vary slightly from the values given owing to orbit and sampling variations.

$$\tau_{21} = 0.0688 + 0.00283\mathrm{TB}_{\mathrm{WVR21}} + 0.00142\mathrm{TB}_{\mathrm{WVR22}} - 0.00060\mathrm{TB}_{\mathrm{WVR31}} - 0.00029T_{\mathrm{A}} \quad (2b)$$

$$\tau_{37} = 0.0546 - 0.00034\mathrm{TB}_{\mathrm{WVR21}} + 0.00018\mathrm{TB}_{\mathrm{WVR22}} + 0.00420\mathrm{TB}_{\mathrm{WVR31}} - 0.00017T_{\mathrm{A}} \quad (2c)$$

$$\mathrm{TB}_{\mathrm{UP18}} = -2.836 + 0.1832\mathrm{TB}_{\mathrm{WVR21}} - 0.0338\mathrm{TB}_{\mathrm{WVR22}} + 0.4418\mathrm{TB}_{\mathrm{WVR31}} + 0.0029T_{\mathrm{A}} \quad (3a)$$

$$\mathrm{TB}_{\mathrm{UP21}} = -1.840 + 1.0492\mathrm{TB}_{\mathrm{WVR21}} + 0.0907\mathrm{TB}_{\mathrm{WVR22}} - 0.1265\mathrm{TB}_{\mathrm{WVR31}} - 0.0014T_{\mathrm{A}} \quad (3b)$$

$$\mathrm{TB}_{\mathrm{UP37}} = 2.866 - 0.1362\mathrm{TB}_{\mathrm{WVR21}} + 0.0351\mathrm{TB}_{\mathrm{WVR22}} + 1.2143\mathrm{TB}_{\mathrm{WVR31}} - 0.0096T_{\mathrm{A}} \quad (3c)$$

where T_{A} is the surface air temperature in kelvins and $\mathrm{TB}_{\mathrm{WVRnn}}$ is the WVR measurement at frequency nn (nn = 21 for 20.7 GHz, nn = 22 for 22.2 GHz, and nn = 31 for 31.4 GHz). The residual RMS errors in (2) are 0.0004, 0.0023, and 0.0011 for the predicted TMR opacities at 18, 21, and 37 GHz. The errors in (3) are 0.041, 0.056, and 0.070 K for the predicted TMR $\mathrm{TB}_{\mathrm{UP}}$ values. The Bermuda database used to generate the regressions was chosen because its path delay range (5–35 cm) brackets the conditions encountered at the four WVR sites. Regressions based on radiosonde data from high- (Chichi Jima) and low- (Norfolk) humidity sites produce TMR brightness temperature predictions which differ by less than 0.3 K from the results of the Bermuda-based regression equations.

By equating $\mathrm{TB}_{\mathrm{DN}}$ and $\mathrm{TB}_{\mathrm{UP}}$ (accurate to 0.1–0.2 K) and using site measurements for T_{S} and T_{A}, WVR-predicted TMR brightness temperatures were computed for each ground site overpass using equations (1)–(3). The accuracy of the predictions depends primarily on the WVR measurement errors and uncertainties in the calm sea emissivity model. The predictions are not sensitive to uncertainties in vapor absorption model line strength or the oxygen absorption component. Absolute calibration accuracies of 0.5 K have been demonstrated in previous field experiments for the WVRs deployed at the TOPEX ground verification sites [*Keihm*, 1991]. This accuracy level contributes uncertainties of ≈0.5, 0.8, and 0.8 K to the TMR brightness temperature predictions at 18, 21, and 37 GHz. The dominant uncertainty in the prediction is due to the uncertainty in the calm sea emissivity, ε. This issue is discussed in the following sections.

Radiosondes

Fifteen radiosonde launch sites were identified which lie near the T/P ground track and from which weather balloons are generally launched twice daily at 1100 and 2300 UTC. They are listed in Table 2 along with the mean path delay at each site during the first 6 months of the T/P mission. Individual path delays during each overpass varied over the range 3–40 cm, providing a wide range of conditions for the intercomparison. (An overpass occurs whenever the point of closest approach of the satellite ground track to the launch site is less than 300 km.) Since path delay estimates derived from the raw radiosonde measurements have the least sensitivity to modeling errors (as opposed to brightness temperature estimates computed using the equation of radiative transfer), they will be compared directly to the path delay retrieved by TMR. Also included in Table 2 is the distance from the launch site to the satellite ground track at the point of closest approach for both ascending and descending nodes of the orbit. Since T/P operates in a non-Sun synchronous orbit the time difference between balloon launch and overpass is fairly uniformly distributed over 0–6 hours. Overpasses for which a launch did not occur within 6 hours were not included in this database.

French Meteorological Office

The European Centre for Medium Range Weather Forecasting provides global estimates of atmospheric water vapor and air temperature fields at discrete vertical levels. These estimates are generated every 6 hours and are constrained by operational satellite data and by the global network of radiosonde profiles measured twice daily [*Lorenc*, 1981, 1986]. Global path delay fields are generated from these data on a 0.5° × 0.5° latitude/longitude grid at 6-hour intervals by the French Meteorological Office (FMO). This field is then spatially interpolated by the Centre de Traitement DORIS POSEIDON to coincide with the TOPEX/POSEIDON ground track [*Stum*, 1994]. These estimates of the path delay are available in parallel with all TMR data on the TOPEX/POSEIDON Geophysical Data Record. Interpolation is not performed in time, but rather the nearest 6-hour value is used.

DMSP SSM/I

The special sensor microwave/imager instrument on the Defense Meteorological Satellite Program Block 5D-2 spacecraft provides brightness temperature images at 19.3, 37.0, and 85.5 GHz with vertical and horizontal polarization and at 22.2 GHz with vertical polarization only, all at a constant incidence angle of 53.1°. SSM/I is a mechanically scanning

Table 3. SSM/I Blackbody Brightness Temperatures in Amazon Rain Forest

Day of Year, 1992	Local Time	TB, Mean ± Standard Deviation, K			Number of Points
		19.3 GHz	22.2 GHz	37 GHz	
281	2206	285.1 ± 2.2	283.4 ± 2.3	281.1 ± 2.5	1506
282	1012	286.2 ± 1.9	284.4 ± 1.8	282.8 ± 1.8	1722
285	1018	286.7 ± 2.3	284.7 ± 2.2	283.1 ± 2.3	1883
287	2219	285.3 ± 1.8	284.1 ± 1.8	281.6 ± 2.0	1571
Average	...	285.8	284.2	282.2	...

Blackbody condition defined as $|TB_v - TB_h| \leq 1.0$ K for both 19.3 and 37.0 GHz. See text for description of latitude and longitude ranges for each of the four passes.

imager with a cross-track swath width of 1394 km and spatial resolution of 54, 49, 32, and 14 km at 19.3, 22.2, 37, and 85.5 GHz, respectively. SSM/I antenna temperature calibration relies on views by the antenna feed horn of a matched load and cold space every 1.9 s. Because of the mechanically scanning geometry, this allows the entire radiometer electronics to be calibrated and greatly reduces the dependence of the calibration accuracy on instrument modeling. Brightness temperature corrections for the antenna sidelobes were verified by aircraft underflights with an SSM/I simulator. Absolute calibration of the SSM/I brightness temperatures is conservatively estimated by *Hollinger et al.* [1990] to be better than ±3 K for all channels used in this study.

SSM/I measurements were used to identify regions of the Amazon rain forest which could be assumed to be approximate black body targets. This was done by requiring that there be a sufficiently small difference between the vertically and horizontally polarized brightness temperatures. Average SSM/I brightness temperatures over these regions were then compared to the average TMR brightness temperatures. SSM/I estimates of integrated water vapor over the open ocean were not intercompared with TMR path delays owing to the unacceptably large temporal decorrelation of the path delay fields between the two data sets.

Intercomparisons of SSM/I with TMR concentrated on days 278–290 of 1992. A number of SSM/I passes in the region of the Amazon rain forest were examined. It was found that a significant percentage of the data lying within 0°–10° south latitude and 60°–70° west longitude had little polarization signature. Specifically, ascending passes were examined on day 281 at 0103–0109 UTC (corresponding to 0–10S, 61.3–63.6W) and day 287 at 0116–0122 UTC (0–10S, 64.4–66.7W). Descending passes were examined on day 282 at 1309–1315 UTC (0–10S, 64.4–66.6W) and day 285 at 1315–1322 UTC (0–10S, 66.0–68.0W). All points were extracted for which the vertical and horizontal brightness temperatures at 19.3 and 37.0 GHz differed by less than 1.0 K. The results are summarized in Table 3.

A small increase in the mean brightness temperature is evident from night to day, but not enough to be explained simply by the typical day and night air temperatures in the region. For example, the mean daily high (daytime) and low (nighttime) surface air temperatures in Manaus, Brazil (≈3S, 60W) for August–December are 306 and 297 K, respectively [*National Geographic*, 1990]. The effective radiating temperature of the rain forest is apparently lower, relative to the surface air temperature, during the day than it is at night. This can be explained by the increase in altitude during the day (and hence the decrease in temperature) of a significant fraction of the atmospheric absorption.

Reference Models

Two models were developed to estimate the hottest and coldest brightness temperatures which TMR was expected to encounter in flight. The hot model is the Amazon rain forest discussed above. Regions of the rain forest with essentially unity emissivity were identified using SSM/I data. The TMR brightness temperatures in these regions can be expected to be slightly lower than the SSM/I values since the atmosphere is more transparent along TMR's nadir path and the land emission is less completely attenuated. Ordinarily, a nadir view over land would result in a higher brightness temperature because the emissivity of land is typically near unity. In this case, however, because of the selective extraction of data over regions with unity atmospheric emissivity along the SSM/I slant path (as evidenced by the complete depolarization of the brightness temperature), the net emissivity along the TMR path is actually reduced slightly.

The coldest brightness temperatures which TMR is expected to encounter occur over open ocean in the subpolar regions under clear, calm conditions. Subpolar locales typically provide the lowest atmospheric water vapor content. Clear conditions remove any emissive contributions from clouds, and calm conditions minimize the excess emissivity generated by ocean surface roughness and foaming. Fortuitously, the coldest brightness temperatures are also the easiest to model accurately. TMR brightness temperatures were simulated for typical subpolar conditions using a number of guidelines. The atmospheric dependence was estimated using a 4-year archive of radiosonde profiles from St. Paul Island (57.2N, 170.2W). The surface emissivity of the ocean was modeled using the Fresnel reflection coefficient and included sea surface salinity and temperature effects on the complex dielectric constant of the water [*Klein and Swift*, 1977]. Sea surface temperature as a function of latitude was derived from regression fits to global advanced very high resolution radiometer (AVHRR/2) maps of the ocean during September and October 1987 [*Halpern et al.*, 1992]. These months were chosen to coincide with the time of TMR intercomparison. Results of the regression fit follow.

$$T_S = 274 + 0.6(60 - \text{LAT}) \quad (4a)$$

for southern latitudes and

$$T_S = 280 + 0.4(60 - \text{LAT}) \quad (4b)$$

for northern latitudes, where T_S is the sea surface temperature in kelvins and LAT is the (positive) latitude in degrees. Equation (4) is valid over the range $40 \leq \text{LAT} \leq 60$. Clear, calm brightness temperatures were computed with variable T_S for the range of atmospheric conditions determined by the St. Paul Island archive. These brightness temperatures (TBff at frequency ff GHz) were then regressed against the path delay (PD) associated with each radiosonde profile and against the assumed sea surface temperature, T_S. The results follow.

$$\text{TB18} = 122.53 + 0.652\text{PD} - 0.176T_S \quad (5a)$$

$$\text{TB21} = 126.90 + 2.155\text{PD} - 0.245T_S \quad (5b)$$

$$\text{TB37} = 154.53 + 0.755\text{PD} - 0.509T_S \quad (5c)$$

where PD is in units of centimeters and T_S in units of degrees Celsius. The RMS residual error between the true brightness temperatures and those predicted by the regression fits was ≤0.5 K at all frequencies over the range of conditions $0 < \text{PD} \leq 7$ cm and $0 \leq T_S \leq 15$°C. The lowest brightness temperatures, associated with the lowest path delays estimated by TMR (typically 2–3 cm), should correspond with the values predicted by (5). This check is useful because the TMR path delay retrieval algorithm tends to produce meaningful (algorithm errors <1 cm) path delay estimates even when there is a substantial bias in the brightness temperatures, provided the bias is approximately common to all three frequencies [*Keihm et al.*, 1994]. Thus satisfactory path delay intercomparisons alone cannot necessarily guarantee accurate brightness temperature calibration. It should also be noted that uncertainties in the water vapor line strength will have only a minimal effect on the accuracy of the brightness temperatures predicted by (5). Errors in the line strength amount to relative errors in the component of the brightness temperature due to the water vapor. Thus, for a condition of PD = 7 cm, uncertainty in the line strength at the 5% level will result in TB model errors of only ≈0.2, 0.8, and 0.3 K at 18, 21, and 37 GHz.

4. Corrections to Instrument Calibration

Bias Correction

Initial intercomparisons between TMR and the various sources of ground truth immediately after launch indicated very large biases (6–12 K over the three frequencies) in the brightness temperatures. The biases were generally consistent using each of the sources of ground truth. For example, the lowest brightness temperatures measured by TMR (in the subpolar regions) were 6–12 K lower than the lowest physically possible values, as determined from (5). Likewise, WVR-predicted TMR brightness temperatures at somewhat higher levels were also 6–12 K above those measured by TMR. The source of a significant portion of the bias was identified as processing errors in the preflight thermal/vacuum (T/V) data analysis. Two problems with the original reduction of the T/V data were corrected. The thermistor calibration coefficients used to measure the temperature of the cold sky calibration horn target were incorrect. Using the correct coefficients raised the cold sky target temperature by several degrees but did not account for the large biases in the in-flight brightness temperatures. However, this correction has been made in the revised processing reported here. Part of the T/V data, which was used to calibrate the instrument's sensitivity to the cold sky brightness temperature, was found to be unusable owing to large temperature gradients present in the cold sky target. This problem was determined to account for almost all of the bias seen in the flight data at the lower end of the range of brightness temperatures. It was corrected by identifying other T/V data taken when the cold sky target was at a stable temperature.

T/V data processing requires that a number of free parameters, associated with the losses and reflections in the on-board TMR calibration hardware, be estimated using a multilinear regression fit to T/V data taken under a wide range of operating temperatures and temperature gradients [*Ruf et al.*, 1994]. A useful figure of merit for the regression fit is the RMS residual error between the antenna temperature measured by TMR and the physical temperature of a target absorber placed over the feed horn of the radiometer. With the revised T/V processing, the RMS error is 0.24, 0.24, and 0.19 K at 18, 21, and 37 GHz. This represents the accuracy of the antenna temperature calibration algorithm for tracking variations in temperature of the absorber target. It doesn't necessarily measure the overall accuracy of the antenna temperature calibration in-flight. Small errors can be expected to result from such effects as backlobe contributions to the antenna feed, nonunity emissivity of the absorber target, and differences between the arithmetic average of the temperature sensors installed in the absorber and the beam-averaged effective radiating temperature of the absorber. It is these errors that the in-flight comparisons are intended to correct.

After revision of the T/V processing, biases in the TMR brightness temperatures, as inferred from the WVR data, were reduced to +0.6 K (TMR low), −0.7 K (TMR high), and −0.1 K (TMR high) at 18, 21, and 37 GHz. These values are derived from the average of 17 overpasses of WVR sites for which the skies were clear, the winds were ≤7 m/s, and horizontal variations in the TMR TB measurements were minimal. A scatterplot of the intercomparison data between the WVR-predicted TMR brightness temperature and the TMR data itself (prior to the final gain correction) is shown in Figure 3. These biases have been incorporated into the antenna temperature calibration algorithm as constant offsets. Their significance pertains to the relative channel-to-channel corrections which most directly impact the path delay retrieval algorithm. The derived individual channel absolute offsets are uncertain to a level of a few Kelvin owing to uncertainty in the effective emissivity of the calm sea. The derived relative offsets, however, are much less affected by the emissivity modeling uncertainty. Application of the final instrument gain corrections (described in the following section) yields TMR brightness temperatures which are elevated 2–3 K above the calm sea model predictions. The authors conjecture that this may be due not to errors in TMR calibration but rather to a deficiency in the model used for the ocean surface emissivity. The ocean surface is modeled as a perfect dielectric half space, with emissivity determined solely by the Fresnel reflection characteristics at the interface. There is some evidence that the true ocean surface emissivity never drops down all the way to the ideal Fresnel condition, even under calm wind "glassy" conditions [*Stogryn*, 1967; *Bespalova et al.*, 1981; *Gaydanskiy et al.*, 1988]. In addition, inconsistencies have

been noted between various models for the dependence of the dielectric constant of ocean water on temperature and salinity [*Wentz*, 1992]. These issues all point to an uncertainty in the calm water emissivity of the ocean which could account for the 2–3 K discrepancy observed here. Constraints on the calm sea emissivity, based on TMR/WVR comparisons, will be explained further using a full year of ground truth data [*Keihm and Ruf*, 1994].

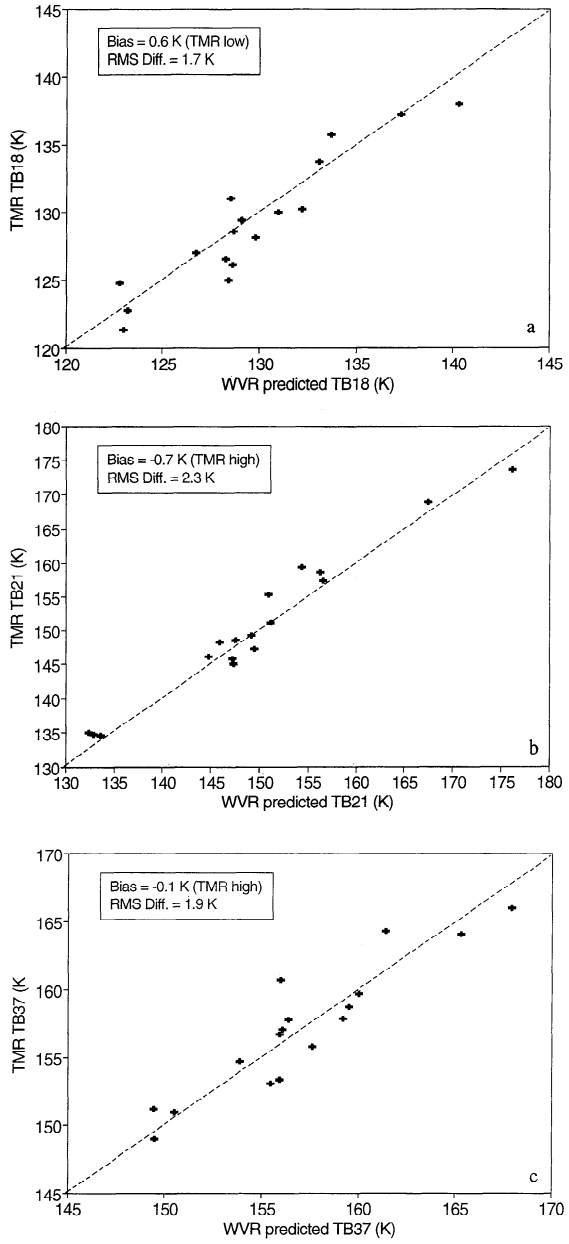

Figure 3. Scatterplot of water vapor radiometer (WVR)-predicted versus actual TMR brightness temperature data before the bias and gain corrections are made to the TMR calibration but after the thermal/vacuum (T/V) processing errors were corrected for (a) TB_{18}, (b) TB_{21}, and (c) TB_{37}. The WVR measurements of downwelling atmospheric brightness temperature and total atmospheric opacity are used to infer the TMR data by including a model for the ocean surface emissivity. This is done under cloudless, low-wind (≤7 m/s) conditions to minimize model dependent errors.

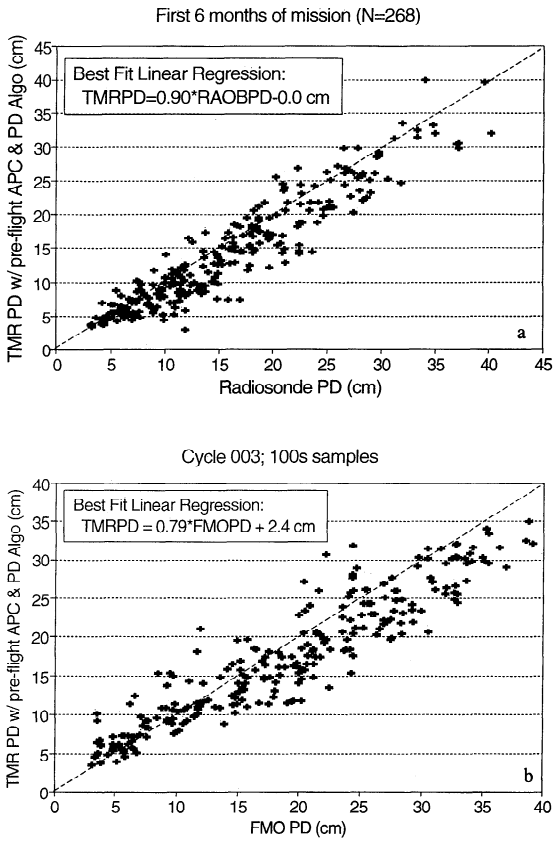

Figure 4. Scatterplot of independent sources of path delay measurements against TMR-derived path delay, with TMR calibration in a state similar to that for Figure 3. (a) Radiosonde path delay for 268 overpasses within 300 km and 6 hours of balloon launch. Data includes all clear, calm, cloudy, and windy conditions. (b) French Meteorological Office (FMO) path delay interpolated in space to coincide with TMR data. Data includes samples of open ocean measurements taken every 100 s during days 290–301 of 1992 (T/P cycle 003).

Gain Correction

A significant gain error was indicated by all pertinent sources of ground truth. These sources can be divided into two classes, path delay and brightness temperature measurements. Comparisons between TMR and the radiosonde data revealed relative errors in path delay of ≈10%. Comparisons with the FMO data revealed relative errors of ≈20%. These errors increased with increasing path delay, with TMR estimates of path delay becoming increasingly low. Scatterplots of TMR path delay against radiosonde and FMO path delay with this relative error are shown in Figure 4. As noted above, possible causes of path delay relative errors include both water vapor line strength errors and instrument calibration gain errors.

The instrument gain error component was determined by evaluation of the highest TMR brightness temperatures, at which gain errors have the largest effect. Comparisons between the Amazon rain forest black body SSM/I brightness temperatures and the TMR measured brightness temperatures were made by averaging TMR data into eight bins. The TMR data over days 278–290 of 1992 were separated into four latitude and longitude regions: (1) 0–5S, 65–70W;

Table 4. TOPEX/POSEIDON Microwave Radiometer TBs in Amazon Rain Forest Before Gain Correction

Latitude/Longitude, Range	Day/Night	TB, Mean ± Standard Deviation, K			Number of Points
		18 GHz	21 GHz	37 GHz	
0–5S, 65–70W	day	272.9 ± 4.2	273.3 ± 3.1	273.5 ± 4.3	90
0–5S, 65–70W	night	273.2 ± 2.6	273.3 ± 1.9	273.7 ± 3.0	58
5–10S, 65–70W	day	273.7 ± 0.8	273.6 ± 0.8	274.1 ± 0.9	92
5–10S, 65–70W	night	276.7 ± 1.2	275.7 ± 1.0	276.1 ± 1.5	94
0–5S, 60–65W	day	265.2 ± 7.4	267.1 ± 5.8	267.7 ± 7.0	78
0–5S, 60–65W	night	272.1 ± 5.0	273.9 ± 3.4	273.9 ± 4.4	47
5–10S, 60–65W	day	273.3 ± 2.7	272.7 ± 2.1	273.7 ± 2.9	93
5–10S, 60–65W	night	275.3 ± 2.6	276.0 ± 2.2	276.6 ± 3.2	47

Data are extracted from days 278–290 of 1992. Day range is 0600–1800 LT; night range is 1800–0600 LT. TMR brightness temperatures calibrated assuming mean on-Earth far sidelobe brightness temperature of 280 K [*Janssen et al.*, 1994].

(2) 5–10S, 65–70W; (3) 0–5S, 60–65W; and (4) 5–10S, 60–65W. Data over each region was additionally separated into day (0600–1800 LT) and night (1800–0600 LT) overpasses. The brightness temperature measurements over each bin are summarized in Table 4. The differential polarization technique used to identify black body regions of the rain forest with the SSM/I data cannot be used here since TMR operates with a single polarization and in the nadir direction, at which the land emission is unpolarized. However, the standard deviation of the TMR brightness temperatures over each bin gives some indication of land contamination, since most variability in the brightness temperature can be assumed to come from the surface. For this reason the (5–10S, 65–70W) region in Table 4 is judged to be the most uniformly black body in behavior. Furthermore, the standard deviations at night tend to be approximately equal to or less than those in the day for all four regions. This can be explained as a corollary to the day/night discussion given above regarding the SSM/I rain forest data, for which the effective radiating temperature of the atmosphere is more closely coupled to the surface air temperature during the night. In the case of TMR measurements the nighttime air can be regarded as less variable over the ranges of latitude and longitude considered. For these reasons the (5–10S, 65–70W) nighttime data will be used as the TMR point of comparison with the SSM/I data.

Comparisons between the specified averaged TMR and SSM/I rain forest data reveal offsets of 9.1, 8.5, and 6.1 K (TMR low) at 18, 21, and 37 GHz. (Here we have assumed that the 18/19.3 and 21/22.2 brightness temperatures are equal, since the near-unity emissivity of the rain forest allows the water vapor absorption spectrum to have only a weak effect on the brightness temperature.) Using the subpolar model intercomparison as a tie point for the TMR gain calibration, this indicates an instrument gain error of 5.6, 5.3, and 4.6% at 18, 21, and 37 GHz. Several points of qualification should be noted regarding this analysis. The subpolar model tie point is based on an ideal Fresnel condition at the ocean surface and so may be in error by 1–3 K, as noted above. The assumed equivalence of SSM/I and TMR rain forest measurements may not be exact since the SSM/I antenna beam travels through significantly more atmosphere in its off-nadir orientation. Also, the absolute calibration of SSM/I brightness temperatures has uncertainties of ±3 K, as noted above. All of these factors combine to make the hot (rain forest) and cold (subpolar) calibration points uncertain at the 3–5 K level. However, since these points are 132–164 K apart at the three frequencies, the estimates given here for instrumental gain error can be conservatively regarded as accurate within approximately ±2.5%.

Regarding the cause of the instrument errors, the very low RMS residuals remaining in the T/V test of the antenna temperature calibration suggest that the brightness temperature calibration is a more likely source of the ≈5% gain error. The preflight antenna pattern correction coefficients, as determined from antenna range measurements of the TMR sidelobe levels, directly affect the gain of the instrument calibration. The gain is most sensitive to the fraction of the integrated sidelobes which lies off the Earth (outside of 55° off nadir). An underestimate of this beam fraction would result in an overestimate of the instrument sensitivity to changes in brightness temperature in the nadir direction, since a larger fraction of the beam would then be directed toward nadir. The preflight off-Earth beam fractions were estimated at 0.49, 0.29, and 0.37% at 18, 21, and 37 GHz [*Janssen et al.*, 1994]. These values have been revised to produce the ≈5% gain corrections derived above and to account for approximately half of the 10% gain error in path delay retrievals. The corrected off-Earth beam fractions are 2.03, 2.04, and 1.77%. The most likely cause of this rise in the integrated power pattern beyond the Earth is a last-minute modification to the antenna, made prior to launch but after the antenna range measurements were completed. A full satellite thermal balance test in the T/V chamber indicated that the thermal blanketing of TMR was inadequate. Thermal blankets were added around the collar containing the main reflector's multifrequency feed. These blankets altered the aperture field distribution because the main reflector is only partially offset. The blankets also probably increased the scattering of energy into the far sidelobes of the antenna pattern. While every reasonable effort was made to conform the blankets as closely as possible to the existing feed collar, the increase in power scattered into the far sidelobes is not unexpected.

5. Corrections to Path Delay Algorithm Line Strength Model

The remaining 5% relative path delay error between TMR and the radiosonde and FMO ground truth was corrected by adjusting the strength of the water vapor absorption line. The prelaunch absorption model was based on a modification of *Liebe and Layton*'s [1987] model which utilizes the Van Vleck-Weiskopf line shape. The modification was an 8% increase in the model line strength to match comparison data between radiosondes and WVRs [*Keihm*, 1992] and to match the only available laboratory data which measured the 22.235 GHz absorption feature [*Becker and Autler*, 1946]. The accuracy of radiosonde calibration of the water vapor absorption feature has long been questioned owing to uncertainties in the radiosonde relative humidity measurements, especially at the high and low ends of humidity conditions [*Elliot and Gaffen*, 1991; *Schwartz and Doswell*, 1991]. Resultant estimates of the vapor absorption model accuracy based on radiosonde/WVR comparisons have been in the 5–10% range. There is also evidence of nonlinearities in the absorption versus vapor density relationship [*Hogg and Guiraud*, 1979]. It is therefore quite plausible that our prelaunch model for vapor absorption may be 5% high, producing TMR path delay results which are 5% low. We have therefore revised our absorption model, lowering the line strength by 5%, to eliminate the remaining scale error indicated by the TMR/radiosonde and TMR/FMO comparisons. The resulting model is equivalent to that of *Liebe and Layton* [1987] with a 3% increase in line strength.

It should be pointed out that the entire 10% scale error apparent in the TMR versus ground truth path delay comparisons could have been corrected by a 10% decrease in the assumed absorption model. However, to produce the best possible TMR calibrations in terms of both brightness temperatures and path delay, the correction was split equally between the brightness temperature calibration and the path delay algorithm. As discussed previously, the ≈5% instrument gain corrections produce consistency between the TMR and SSM/I brightness temperature measurements of the Amazon rain forest.

6. Conclusions: Assessment of Brightness Temperature and Path Delay Retrieval Accuracies

Brightness Temperature Accuracy

A quantitative measure of the accuracy of the TMR brightness temperature calibration can be made by comparison with the coincident WVR measurements. Unfortunately, the estimated TMR accuracy can not easily be separated from the 1–3 K uncertainties in the calm sea surface emissivity model. Scatterplots of WVR-inferred TMR brightness temperatures against those measured by TMR, after all the calibration corrections have been made, are shown in Figures 5a–5c for the three TMR frequencies. The bias between the two data sets is 2.3, 2.9, and 2.2 K, with the TMR high at 18, 21, and 37 GHz. Similar biases (2.8, 3.1, and 3.1 K) are observed when comparing the final TMR calibration to the subpolar reference models. The success of the revised T/V calibration, instrument gain corrections, and modified path delay retrieval algorithm in producing agreement with both the Amazon brightness temperature data and

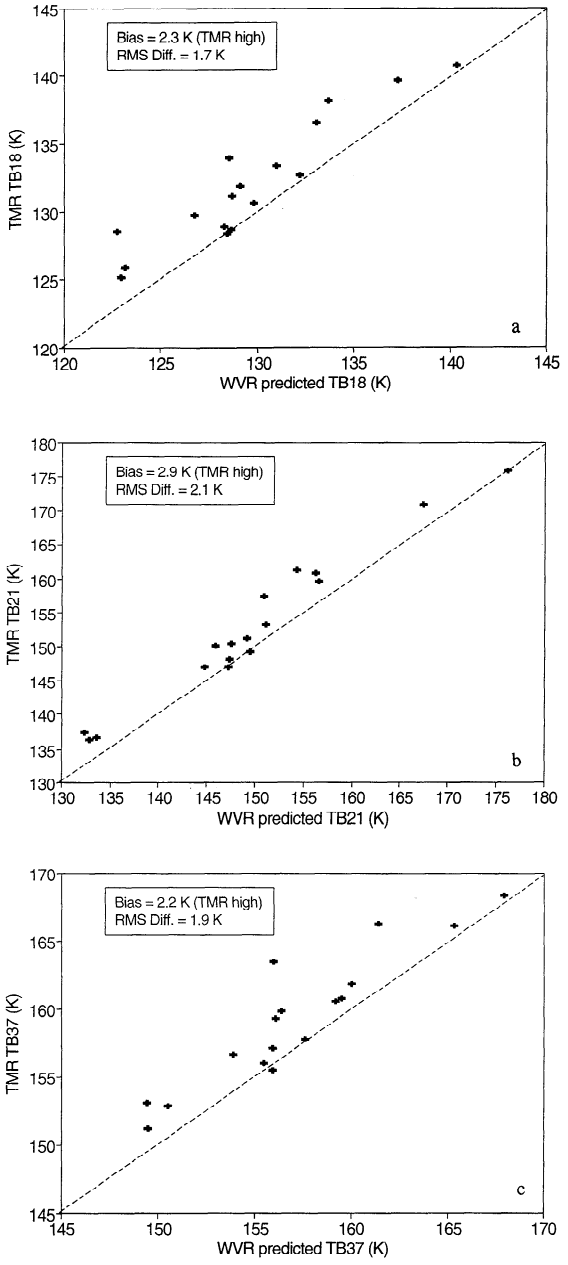

Figure 5. Scatterplot of WVR-predicted versus actual TMR brightness temperatures after all calibration corrections are made for (a) TB_{18}, (b) TB_{21}, and (c) TB_{37}. The 2–3 K offsets can largely be explained by a small increase in the calm sea emissivity above that of the ideal Fresnel condition.

the ground-based path delay results suggests that the open ocean offsets seen in the brightness temperature comparisons are due to a calm sea component which adds ≈0.01 to the Fresnel prediction of the nadir emissivity. As discussed above, previous theoretical and experimental results have suggested the existence of a small 1–3 K nonspecular component of the calm sea nadir flux. However, to the authors' knowledge no previous aircraft or satellite radiometer has demonstrated the absolute calibration accuracy necessary to definitively measure this effect. The TMR data suggests that the calm sea enhancement is 2–3 K over the 18–37 GHz frequency range. This result depends primarily on the accuracy of our SSM/I-based model for the Amazon rain forest

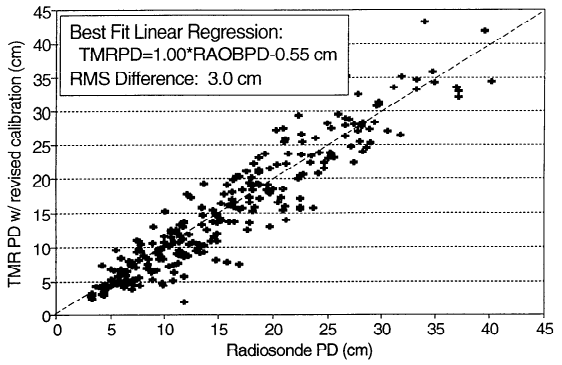

Figure 6. Scatterplot of TMR against radiosonde path delays for the same data set described in Figure 4a, but with all the corrections to the instrument calibration and water vapor line strength incorporated into the TMR data processing.

emission. Assuming that the derived gain corrections may be in error by up to ±2.5%, we estimate the TMR open ocean brightness temperature accuracy to be ±1.5 K.

Path Delay Accuracy

The accuracy of TMR retrievals of path delay is derived primarily from a comparison with the radiosonde database. A scatterplot of TMR and radiosonde path delays is shown in Figure 6 after all instrument calibration and water vapor line strength corrections have been incorporated into the TMR data processing. This data set includes clear, calm weather conditions as well as all cloudy and windy cases experienced during the first 6 months of the mission. Rainy data, as indicated by a TMR liquid water retrieval of ≥1000 μ, have been deleted. The RMS scatter between the two data sets is 3.0 cm. This scatter includes three uncorrelated sources in addition to the TMR error. The RMS error associated with individual radiosonde soundings is estimated to be 0.7 cm [*Alishouse et al.*, 1990]. Analysis of radiosonde errors by other investigators [e.g., *Hoehne*, 1980] reveal patterns of errors in the temperature and humidity measurements which could easily lead to greater than 5% errors in the integrated vapor calculations (approximately 1 cm in mean path delay error for our comparison data set). We adopt the 0.7-cm value for our analysis, a conservative selection in the sense that higher radiosonde errors will yield lower TMR errors for the given TMR-radiosonde comparison data.

Additional errors in the comparisons result from the spatial and temporal decorrelation between the TMR and radiosonde path delay measurements. The spatial effect can be estimated directly from the TMR data. Figure 7 shows the decorrelation as a function of ground track displacement calculated directly from the TMR data for four cycle 002 passes which are representative of the range of typical data. The differences are primarily due to the fraction of cloudy conditions encountered, since variability tends to increase in these regions. Based on averages of the Figure 7 results and a mean TMR-radiosonde separation distance of 150 km, we adopt an error of 2.3 cm for the spatial decorrelation component.

The temporal decorrelation between the TMR and radiosonde measurements is more difficult to evaluate. If we assume that the temporal decorrelation is due to the wind-driven horizontal motion of the path delay field, then the resulting error can be estimated from the spatial decorrelation data of Figure 7. The estimate requires input of the average time separation and wind speed component parallel to the TMR-radiosonde separation vector. For our average TMR-radiosonde time separation of 2.9 hours and mean ocean wind speeds of 10 m/s [*Halpern et al.*, 1992], with average alignment 45° from the separation vector, the time decorrelation error is equivalent to the spatial effect at 73 km separation. From Figure 7 this value is 1.4 cm.

Evaluated as an orthogonal sum which produces the 3-cm residual of the TMR-radiosonde comparison set, the above results yield 1.1 cm for the TMR path delay error. This value is subject to considerable uncertainty because the TMR error is not the dominant error in the radiosonde comparisons. If the spatial decorrelation error is actually 2.1 cm, plausible given the Figure 7 data, then the derived TMR error increases to 1.5 cm. If, on the other hand, the wind speed vector is preferentially aligned east-west, then the time decorrelation error increases to 1.7 cm, yielding a 0.6-cm TMR error.

With no other ground comparisons, the 1.1-cm calculated TMR performance would be subject to approximately ±0.5-cm uncertainty due to the large decorrelation effects. However, in our comparisons of TMR and WVR path delays at the four WVR ground sites, the TMR-minus-WVR residuals are less than 1 cm [*Keihm and Ruf*, 1994], suggesting that the 1.1-cm TMR performance level may actually be a conservative estimate. The large reduction in residuals relative to the TMR-radiosonde comparisons (3 cm) illustrates the advantages of ground-based WVR comparisons, which are time synchronized and at relatively small (≈30 km) separation distances from the satellite ground track.

Path Delay Sensitivity to Clouds and Wind

The mission requirements for TMR included the ability to accurately retrieve path delay under all cloudy and windy conditions, excluding rain. This can be readily demonstrated, since the TMR retrieval algorithm also estimates ocean surface wind speed and integrated cloud liquid water content along with each path delay estimate. (These parameters are used as second-order corrections to the path delay retrieval algorithm itself [*Keihm et al.*, 1994].) In Figures 8a

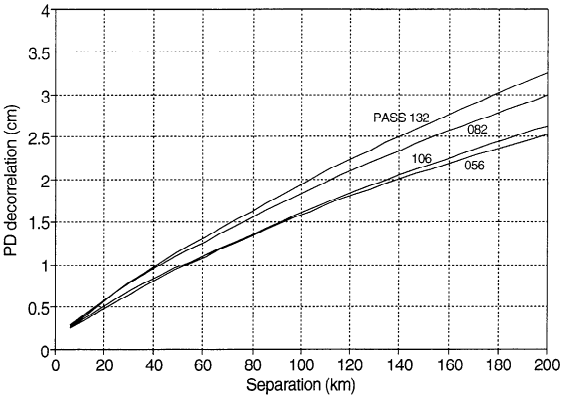

Figure 7. Statistical decorrelation of the TMR path delay with respect to the separation between two points along the satellite ground track. Data from four orbits during cycle 002 of the mission are shown. Differences in the decorrelation are due primarily to differences in the cloud cover.

and 8b, the difference between radiosonde and TMR path delay is plotted against the wind speed and cloud liquid retrieved by TMR. A summary of the RMS scatter and mean difference between the radiosonde and TMR values is given in Table 5 for different subsets of the wind and cloud liquid retrievals. Figure 7 and Table 5 indicate that the RMS accuracy of the TMR path delay retrieval is relatively insensitive to the cloud and wind conditions, thus satisfying the mission requirements. Table 5 also indicates that TMR path delay is not significantly biased under consistently windy or cloudy conditions. This is in marked contrast to the path delay retrieval performance predicted for several two-frequency retrieval algorithms [*Keihm et al.*, 1994]. For example, biases of 2–5 cm are predicted by *Keihm et al.* [1994] with a satellite water vapor radiometer operating at 21 and 37 GHz under surface wind speed conditions of 18–28 m/s. The issue of how many (and which) frequencies are needed to retrieve path delay satisfactorily is timely in light of the current design studies underway for TOPEX Follow On, GEOSAT Follow On II, the EOS Altimeter radiometer, and the ERS-2 radiometer. The presence of large biases in the two-frequency retrieval algorithms does not significantly increase the global RMS error in the path delay retrieval, since high-wind conditions happen relatively infrequently on a global scale. However, such path delay retrieval algorithms, which are designed to minimize global RMS error, can introduce artifacts into the ocean surface topology maps in isolated regions of the globe over which mean surface winds are anomalously high.

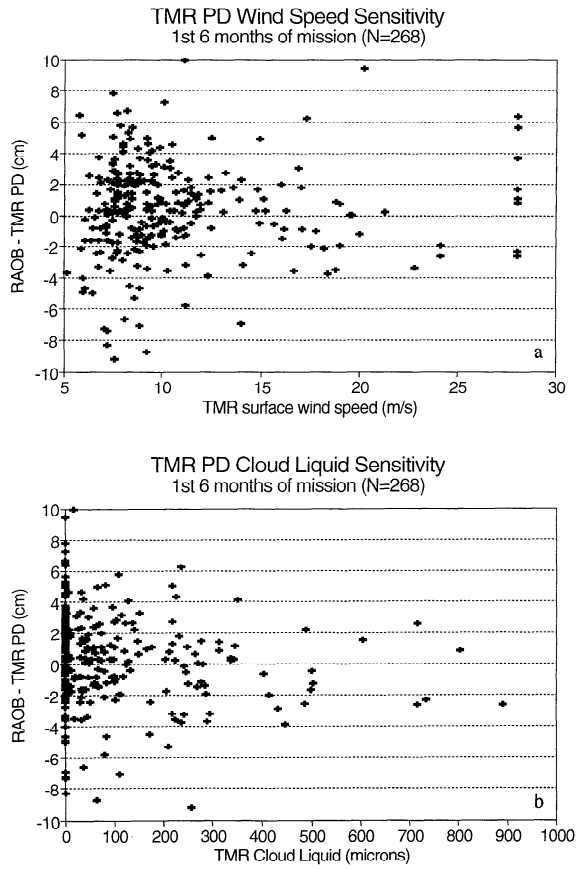

Figure 8. Scatterplot of TMR path delay retrieval error (defined as radiosonde path delay-TMR path delay) against TMR retrievals of (a) ocean surface wind speed and (b) integrated cloud liquid water content.

Table 5. TMR Path Delay Sensitivity to Clouds and Wind

Wind Speed Range, m/s	Cloud Liquid Range, μm	Radiosonde-TMR Path Delay RMS, cm	Average, cm	Number of Samples
All	all	3.00	0.44	268
<8	all	3.34	0.12	74
8–15	all	2.83	0.62	158
>15	all	3.01	0.28	36
All	<50	3.21	0.83	152
All	50–300	2.85	−0.02	94
All	>300	2.06	−0.32	22

Wind speed and cloud liquid are retrieved from TMR brightness temperatures by statistical inversion. The absolute accuracy of these retrievals has not been independently verified, but their performance is expected to be sufficient to differentiate the general classes of weather conditions considered here. RMS and average statistics of the TMR path delay error are based on the data set shown in Figure 6.

Acknowledgments. The authors would like to acknowledge the assistance of several individuals and organizations for their assistance with this work. Texaco generously provided free use of their oil platform Harvest for TOPEX/POSEIDON calibration. The Japanese Local Meteorological Observatories and the Australian Bureau of Meteorology were very helpful in facilitating the WVR deployments at Chichi Jima and Norfolk Island. Alan Tanner of the Jet Propulsion Laboratory maintained the WVRs at Harvest and Lampedusa. Peter Gaiser and Karen St. Germain of the University of Massachusetts operated the WVRs at Chichi Jima and Norfolk Island. Dawn Conway of the Naval Research Laboratory helped with the extraction of pertinent SSM/I data from NRL's DMSP archive. This work presents the results of one phase of research conducted at the Jet Propulsion Laboratory, California Institute of Technology, Pasadena, CA, under contract to the National Aeronautics and Space Administration.

References

Alishouse, J. C., S. A. Snyder, J. Vongsathorn, and R. R. Ferraro, Determination of oceanic total precipitable water from the SSM/I, *IEEE Trans. Geosci. Remote Sens.*, *28*, 811–816, 1990.

Becker, G. E., and S. H. Autler, Water vapor absorption of electromagnetic radiation in the centimeter wavelength range, *Phys. Rev.*, *70*, 300–307, 1946.

Bespalova, Y. A., V. M. Veselov, A. A. Glotov, Y. A. Militskii, V. G. Mirovskiy, L. V. Pokrovskaya, A. Y. Popov, M. D. Rayev, E. A. Sharkov, and V. S. Etkin, Sea-ripple anisotropy estimates from variations in polarized thermal emission of the sea (in Russian), *Dokl. Akad. Nauk SSSR*, *246*(6), 1482–1485, 1979. (*Oceanology*, Engl. Transl., *21*, 213-217, 1981.)

Elliot, W. P., and D. J. Gaffen, On the utility of radiosonde humidity archives for climate studies, *Bull. Am. Meteorol. Soc.*, *72*, 1507–1520, 1991.

Francis, E. A., Calibration of the Nimbus 7 SMMR, M.S. thesis, 248 pp., Dept. of Oceanogr., Oregon State Univ., Corvalis, Oreg., 1987.

Gaydanskiy, S. I., V. Y. Gershenzon, and V. K. Gromov, Detection of surface manifestations of internal waves in the ocean by microwave radiometry, *Izv. Acad. Sci. USSR Atmos. Oceanic Phys.*, Engl. Transl., *24*, 731–735, 1988.

Halpern, D., V. Zlotnicki, J. Newman, D. Dixon, O. Brown, and F. Wentz, An atlas of monthly mean distributions of Geosat sea surface height, SSM/I surface wind speed, AVHRR/2 sea surface

temperature, and ECMWF surface wind components during 1987, *Pub. 92-3*, Jet Propul. Lab., Pasadena, Calif., 1992.

Hoehne, W. E., Precision of National Weather Service upper air instruments, *NOAA Tech. Memo. NWS T&ED-16*, 23 pp., U.S. Govt. Print. Office, Washington, D. C., 1980.

Hogg, D. C., and F. O. Guiraud, Microwave measurements of the absolute values of absorption by water vapour in the atmosphere, *Nature*, *279*, 408–409, 1979.

Hollinger, J. P., J. L. Pierce, and G. A. Poe, SSM/I instrument evaluation, *IEEE Trans. Geosci. Remote Sens.*, *28*, 781–790, 1990.

Janssen, M. A., C. S. Ruf, and S. J. Keihm, TOPEX/POSEIDON microwave radiometer (TMR), II, Antenna pattern correction and brightness temperature algorithm, *IEEE Trans. Geosci. Remote Sens.*, in press, 1994.

Keihm, S. J., Water vapor radiometer intercomparison experiment: Platteville, Colorado, March 1–14, 1991, Final report prepared for Battelle, Pacific Northwest Laboratories, *JPL Int. Doc. D-8898*, Jet Propul. Lab., Pasadena, Calif., 1991.

Keihm, S. J., Atmospheric absorption from 20-32 GHz: Radiometric constraints on the vapor and oxygen components, in *Proceedings of Specialist Meeting on Microwave Radiometry and Remote Sensing Applications*, edited by E. R. Westwater, pp. 211–218, NOAA Environmental Research Laboratory, Boulder, Colo., 1992.

Keihm, S. J., and C. S. Ruf, The role of water vapor radiometers in the TOPEX microwave radiometer in-flight calibration, *J. Mar. Geod.*, in press, 1994.

Keihm, S. J., M. A. Janssen, and C. S. Ruf, TOPEX/POSEIDON microwave radiometer (TMR), III, Wet troposphere range correction algorithm and pre-launch error budget, *IEEE Trans. Geosci. Remote Sens.*, in press, 1994.

Klein, L. A., and C. T. Swift, An improved model for the dielectric constant of sea water at microwave frequencies, *IEEE J. Oceanic Eng.*, *OE-2*, 104–111, 1977.

Liebe, H. J., and D. H. Layton, Millimeter-wave properties of the atmosphere: Laboratory studies and propagation modeling, *NTIA Rep. 87-24*, Natl. Telecom. and Inform. Admin., Boulder, Colo., 1987.

Linn, E. I., TOPEX Microwave Radiometer: Thermal design verification test and analytical model validation, in AIAA 30th Aerospace Sciences Meeting and Exhibit, Reno, Nevada, *AIAA Pap.*, *92-0816*, 1992.

Lorenc, A. C., A global three dimensional multivariate statistical interpolation scheme, *Mon. Weather Rev.*, *109*, 701–721, 1981.

Lorenc, A. C., Analysis methods for numerical weather prediction, *Q. J. R. Meteorol. Soc.*, *112*, 1177–1194, 1986.

Milman, A. S., and T. T. Wilheit, Sea surface temperature from the scanning multichannel microwave radiometer on Nimbus 7, *J. Geophys. Res.*, *90*(C6), 11,631–11,641, 1985.

National Geographic Society, *National Geographic Atlas of the World*, 6th ed., Washington, D. C., 1990.

Ruf, C. S., S. J. Keihm, and M. A. Janssen, TOPEX/POSEIDON microwave radiometer (TMR), I, Instrument description and antenna temperature calibration, *IEEE Trans. Geosci. Remote Sens.*, in press, 1994.

Schwartz, B. E., and C. A. Doswell III, North American rawinsonde observations: Problems, concerns, and a call to action, *Bull. Am. Meteorol. Soc.*, *72*, 1885–1896, 1991.

Stewart, R., L.-L. Fu, and M. Lefebvre, Science opportunities from the TOPEX/POSEIDON mission, *JPL Publ. 86-18*, Jet Propul. Lab., Pasadena, Calif., 1986.

Stogryn, A., The apparent temperature of the sea at microwave frequencies, *IEEE Trans. Antennas Propag.*, *AP-15*, 278–286, 1967.

Stum, J., A comparison between TOPEX microwave radiometer, ERS-1 microwave radiometer, and European Centre for Medium-Range Weather Forecasts derived wet tropospheric corrections, *J. Geophys. Res.*, this issue.

Swanson, P. N., and A. L. Riley, The Seasat scanning multichannel microwave radiometer (SMMR): Radiometric calibration algorithm development and performance, *IEEE J. Ocean. Eng.*, *OE-5*, 2, 116–124, 1980.

Wentz, F. J., Measurements of oceanic wind vector using satellite microwave radiometers, *IEEE Trans. Geosci. Remote Sens.*, *30*, 960–972, 1992.

M. A. Janssen, Jet Propulsion Laboratory, California Institute of Technology, Pasadena, CA 91109.

S. J. Keihm, Jet Propulsion Laboratory, Pasadena, CA 91109.

C. S. Ruf, Department of Electrical Engineering, Pennsylvania State University, University Park, PA 16802.

B. Subramanya, NASA Goddard Space Flight Center, Code 925, Greenbelt, MD 20771.

(Received November 29, 1993; revised March 15, 1994;
accepted March 15, 1994.)